



**HAL**  
open science

# Laser energy deposition with ring-Airy beams beyond kilometer range in the atmosphere

Long Zou, Chen Sun, Jin Yu, Arnaud Couairon

► **To cite this version:**

Long Zou, Chen Sun, Jin Yu, Arnaud Couairon. Laser energy deposition with ring-Airy beams beyond kilometer range in the atmosphere. *Physical Review A*, 2023, 108 (2), pp.023524. 10.1103/PhysRevA.108.023524 . hal-04309379


**HAL Id: hal-04309379**

**<https://hal.science/hal-04309379>**

Submitted on 27 Nov 2023

**HAL** is a multi-disciplinary open access archive for the deposit and dissemination of scientific research documents, whether they are published or not. The documents may come from teaching and research institutions in France or abroad, or from public or private research centers.

L'archive ouverte pluridisciplinaire **HAL**, est destinée au dépôt et à la diffusion de documents scientifiques de niveau recherche, publiés ou non, émanant des établissements d'enseignement et de recherche français ou étrangers, des laboratoires publics ou privés.

**Laser energy deposition with ring-Airy beams beyond kilometer range in the atmosphere**Long Zou <sup>1,2</sup>, Chen Sun,<sup>1</sup> Jin Yu,<sup>1,\*</sup> and Arnaud Couairon<sup>2,†</sup><sup>1</sup>*School of Physics and Astronomy, Shanghai Jiao Tong University, Shanghai 200240, China*<sup>2</sup>*CPHT, CNRS, Ecole Polytechnique, Institut Polytechnique de Paris, F-91128 Palaiseau, France*

(Received 20 April 2023; accepted 15 August 2023; published 30 August 2023)

Controlled deposition of high laser-power density at remote distances still remains a challenge. Previous experimental works using terawatt peak-power laser systems to initiate filamentation at distances of hundreds or even thousands of meters in the atmosphere have documented limited control on laser energy deposition due to the effects of diffraction and turbulence. In this work, we demonstrate a promising scenario for the projection of high power densities at kilometeric distances in air, which requires multiple-gigawatt laser pulses reshaped into ring-Airy beams. We show that a power distribution over a relatively large primary ring accompanied by the inward power flux characterizing a ring-Airy beam limits the occurrence of nonlinear effects to the vicinity of the focal point. Close to focus, self-focusing sets in, which accelerates the convergence process of the beam. We quantify the influence of self-focusing on the focal shift and propose an empirical law that fits our numerical simulation results for the position of the nonlinear focus as a function of the input power and the apodization factor of the ring-Airy beam. We show that once the intensity of the beam exceeds the ionization threshold of air, a short filament is generated whose power content rather accurately corresponds to the critical power for self-focusing, independent of the input parameters.

DOI: [10.1103/PhysRevA.108.023524](https://doi.org/10.1103/PhysRevA.108.023524)**I. INTRODUCTION**

About a decade ago, finite-energy ring-Airy beams were proposed as prototypical wave forms that exhibit enhanced autofocusing contrast and abruptness in the case of long focal lengths [1,2]. Due to their cubic radial phase distribution, ring-Airy beams are able to undergo autofocusing featuring an acceleration of the focusing rate around the focal point on axis, without assistance from an external lens or nonlinearity during propagation. The distribution of energy over the ring beam profile is one of the key ingredients allowing for the contrast enhancement in the region of the autofocus, hereafter called the focal region. The autofocusing property of ring-Airy beams is preserved in the nonlinear regime of powerful laser beams, opening the way to applications ranging from filamentation [3–5] and high-harmonic generation [6] to terahertz generation [7], biomedical manipulation and micromachining [8–11], and multiphoton polymerization [12]. Due to their ring structure, ring-Airy beams can also be focused beyond obstacles smaller than their ring beam radius, opening the way to applications where the target focal point lies behind an object. In addition, ring-Airy beams exhibit self-healing characteristics similar to those of Bessel beams, allowing for their reconstruction after encountering an obstacle [13]. Properties related to the vorticity [14–17], coherence [18–20], manipulation of nanoparticles [21–23] and polarization [24–26] have also been studied for different types of ring-Airy beams.

The linear propagation dynamics and control of ring-Airy beams using different modulation methods have been studied extensively. Theoretically, it is possible to precisely control the characteristics of a ring-Airy beam (trajectory of the peak intensity, amplitude, and width) and its focusing characteristics by carefully engineering the wave front [27]. By modulating the spatial spectrum using a Gaussian function, the focal intensity is enhanced, and the focal size is shortened, while the focal position remains virtually unchanged [28]. A similar result is obtained by applying a Bessel modulation directly to the spatial profile of the ring-Airy beam, leading to a shorter focal length than for an unmodulated beam [11]. The focal region can also be tailored by applying an additional conical phase in paraxial [29,30] and nonparaxial [31] regimes. Assisted by nonparaxial energy flow, the paraxial abrupt autofocusing leads to a stronger enhancement in focal peak intensity, approaching the wavelength limit [32]. Beams with different initial emission angles can be superimposed to focus simultaneously on the first and second peaks, thus influencing both the focal positions and intensities [33]. However, only a few works concern the nonlinear evolution of ring-Airy beams. The filamentation dynamics and corresponding wavefront evolution beyond the autofocus of a ring-Airy beam are described in [5,34]. The nonlinear propagation of ring-Airy beams with different truncation factors was also investigated in [35]. To the best of our knowledge, previous research works have mainly focused on propagation, whether it is linear or nonlinear, and regularization of ring-Airy beams over short distances. Long-distance propagation of ring-Airy beams in air still has to be explored in detail to identify the characteristics that could be useful in potential atmospheric applications.

In this work, we focus on the nonlinear propagation dynamics of intense finite-energy ring-Airy beams in the

\*jin.yu@sjtu.edu.cn

†arnaud.couairon@polytechnique.edu

atmosphere at kilometer scales. We have thoroughly investigated the evolution of the ring-Airy beam wave front as a function of the input power through numerical simulations, with the goal of delivering the highest intensity in the focal region. Before the beam reaches the focal region, its intensity remains low enough for the beam to propagate almost linearly. However, when the first ring of the beam converges on the central axis, the sudden accumulation of inward energy flow leads to a large increase in light intensity, causing significant nonlinearity. A previous study showed that the enhancement of maximum intensity or intensity contrast exceeds two orders of magnitude in linear propagation [1]. Our results show that the intensity contrast can be further amplified by the Kerr nonlinearity in the final stage of autofocusing, leading to an enhancement of more than four orders of magnitude. The position of the nonlinear focus is determined by the total power and its ratio to the power content contained in the primary ring. An empirical formula was given in Ref. [5] that predicts the nonlinear focus shift for propagation of a few centimeters, on the basis of which we derived a modified version that is valid up to kilometer scales. Regardless of the focus position, the induced filaments around the focus are almost invariant to the input condition. Their lateral size is about 100  $\mu\text{m}$ , where the deposited power in the filament is always a measure of the critical power of the air.

## II. NONLINEAR PROPAGATION OF A RING-AIRY BEAM IN AIR

### A. Initial condition: Finite-energy ring-Airy beam

The laser pulse is assumed to be linearly polarized and described by the electric field envelope of the input beam. In our simulations, it is given by

$$\mathcal{E}(z=0, r) = \mathcal{E}_0 \text{Ai}\left(\frac{r_0 - r}{w_0}\right) \exp\left(\alpha \frac{r_0 - r}{w_0}\right), \quad (1)$$

where  $\text{Ai}(\cdot)$  is the Airy function [36,37],  $r$  is the radial coordinate,  $r_0$  and  $w_0$  are the radius and scaling parameter of the primary ring, and  $\alpha$  denotes the truncation factor leading to a finite-power ring-Airy beam. Its total input power is calculated as  $P_{\text{in}} = 2\pi \int_0^\infty |\mathcal{E}(r)|^2 r dr = |\mathcal{E}_0|^2 w_0^2 \sqrt{\pi/(2\alpha)} \exp(2\alpha^3/3) [r_0/w_0 + (1 - 4\alpha^3)/(4\alpha)]$  [1]. Everywhere throughout the paper, the intensity of the field envelopes  $|\mathcal{E}|^2$  is expressed in watts per square centimeter. When the beam propagates forward, an inward energy flow slowly develops that is responsible for the autofocusing property of the beam. In linear propagation, the radial position of the peak intensity follows a quasiparabolic trajectory until it enters the focal region where the primary ring radius becomes comparable to its width, leading to the abrupt increase of the peak intensity. The position of the autofocus is at  $f = 4z_{\text{R}}\sqrt{r_0/w_0 + 1}$ , with the Rayleigh length  $z_{\text{R}} \equiv k_0 w_0^2/2$  [1,2,5,30]. The intensity profile of a ring-Airy beam is shown in Fig. 1. Experimental generation of a ring-Airy beam can be achieved by using a spatial light modulator, as described in detail in Refs. [2,5].

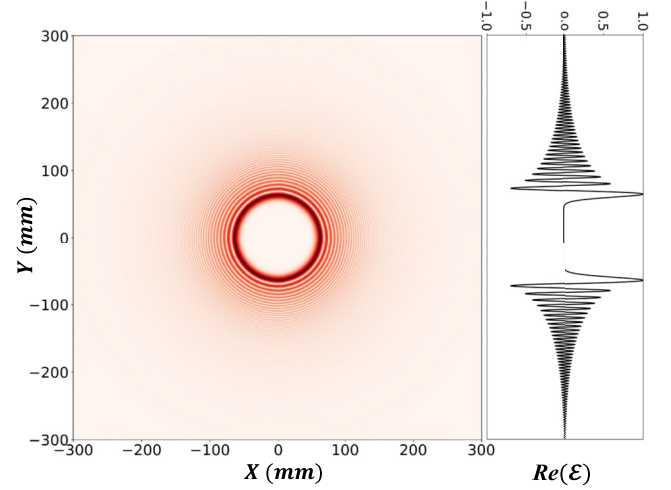


FIG. 1. Normalized intensity plot of a finite-energy ring-Airy beam, with  $w_0 = 4$  mm,  $r_0 = 60$  mm,  $\alpha = 0.05$ , and  $z = 0$ .

### B. Nonlinear wave-propagation equation

The nonlinear evolution of the electric field envelope is described by an extended nonlinear Schrödinger equation (NLSE). Under the paraxial and slowly varying envelope approximations, the NLSE reads

$$\begin{aligned} \partial_z \mathcal{E} = & \frac{i}{2k} \Delta_\perp \mathcal{E} + ik_0 n_2 |\mathcal{E}|^2 \mathcal{E} - \frac{\beta_K}{2} |\mathcal{E}|^{2K-2} \mathcal{E} \\ & - \frac{\sigma}{2} (1 + i\omega_0 \tau_c) \rho \mathcal{E}, \end{aligned} \quad (2)$$

where the terms on the right-hand side of Eq. (2) account for diffraction, the optical Kerr effect, multiphoton absorption (MPA), and plasma defocusing, respectively. We also work in the frozen-pulse approximation; that is, the electric field  $\mathcal{E}(r, z)$  is assumed to represent the central time slice of a laser pulse whose temporal profile is and remains Gaussian  $\exp(-t^2/t_p^2)$  with duration  $t_p$ . This imposes limitations discussed below. Equation (2) then describes the evolution of the beam profile of the laser pulse in the reference frame of the moving pulse. The parameters  $n_0$  and  $n_2$  are the refractive index and nonlinear index coefficient,  $\omega_0$  is the central frequency of the carrier wave,  $k \equiv n_0 k_0 = n_0 \omega_0/c$  is the wave number, and  $\beta_K$  is the  $K$ -photon absorption coefficient. The cross section for inverse bremsstrahlung [38]

$$\sigma = \frac{k_0}{\rho_c} \frac{\omega_0 \tau_c}{1 + \omega_0^2 \tau_c^2} \quad (3)$$

is a function of the electron collision time  $\tau_c$ , and  $\rho_c \equiv \omega_0^2 \epsilon_0 m/e^2$  is the critical plasma density beyond which an overdense plasma turns opaque with respect to electromagnetic radiation of frequency  $\omega_0$ . The electron number density  $\rho$  is governed by the rate equation

$$\partial_t \rho = \frac{\sigma}{E_g} \rho \mathcal{I} + \frac{\beta^{(K)} \mathcal{I}^K}{K \hbar \omega} - a \rho^2, \quad (4)$$

describing cascade and multiphoton ionization, where  $E_g$  is the ionization potential, as well as radiative recombination [39]. In keeping with our frozen-pulse approximation, the electron density  $\rho$  is calculated at every  $(z, r)$  by solving

TABLE I. Parameters used for simulations in air for a beam at 800 nm.

Parameter	Value
$w_0$ (mm)	4
$r_0$ (mm)	60
$\alpha$	0.05
$n_2$ (m <sup>2</sup> /W)	$3.2 \times 10^{-23}$
$\tau_c$ (fs)	350
$E_g$ (eV)	12.1
$K$	8
$\beta^{(K)}$ (m <sup>13</sup> /W <sup>7</sup> )	$4 \times 10^{-121}$
$a$ (m <sup>3</sup> /s)	$5.0 \times 10^{-13}$

Eq. (4) for a pulse whose maximum intensity is  $|\mathcal{E}(r, z)|^2$  and whose temporal profile is a Gaussian function  $\exp(-t^2/t_p^2)$ .

A split-step method thoroughly described in [40] is used to solve the NLSE numerically. Parameters used in our simulations in air are summarized in Table I. The critical power for self-focusing in air,  $P_{cr} = 3.72\lambda^2/8\pi n_0 n_2$  [41], is about 3.2 GW for laser wavelength  $\lambda = 800$  nm. The primary ring parameters  $w_0$  and  $r_0$  are chosen to set the linear autofocus distance at 1 km, precisely, at  $f \approx 1005.3$  m.

Our main goal is to determine how to control laser energy deposition at kilometric distances by acting on the autofocusing property of a ring-Airy beam. The framework of this study is thus set by the frozen-pulse approximation, which, besides accelerating the computation, limits the validity of our results to cases where the pulse profile effectively undergoes limited changes during propagation. Up to the focal region, group-velocity dispersion is the main effect acting on the pulse-profile evolution. For input pulse duration  $t_p = 250$  fs, the characteristic length of the group-velocity dispersion (GVD) is  $L_{GVD} = t_p^2/(2k_0^{(2)}) \approx 1562.5$  m (dispersive coefficient in air  $k_0^{(2)} = 20$  fs<sup>2</sup>/m). A comparison between  $L_{GVD}$  and the linear focus  $f$  justifies the neglect of dispersion in the NLSE [Eq. (2)] [42], which amounts to keeping the pulse duration constant in our calculation. Furthermore, we can prechirp the input beam to compensate for the dispersion during propagation in a real experiment.

### III. RESULTS AND DISCUSSION

Our choice of parameters was governed by the goal of reaching the highest possible intensity in the focal region while controlling its position. Linear propagation of a ring-Airy beam shows that the position of the focus corresponds to the convergence and merging of the primary ring into a bell-shaped beam with an on-axis intensity peak. In order to enhance the abruptness of the convergence by beam self-focusing, we selected a parameter set allowing us to increase the power of the primary ring. Our simulations led to various situations where the ring-Airy beam could not properly focus: (i) A too high peak intensity immediately leads to ionization of air and associated nonlinear losses. (ii) A too high beam power leads to Kerr self-focusing and beam collapse in the form of a ring that presumably corresponds to the universal G-profile [43], followed by diffraction. Our choice of

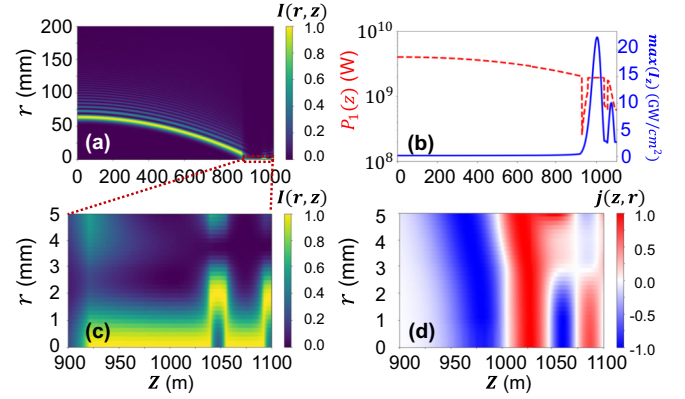


FIG. 2. Linear propagation of a ring-Airy beam with  $P_{in} \leq P_{cr}$ . Evolution of (a) the normalized intensity profile, (b) the power content in the primary ring (red dashed curve) and the on-axis intensity (blue solid curve), (c) the normalized intensity profile, and (d) the energy current density around the autofocus. The energy current is defined as  $j_{\perp}(z, r) = \frac{1}{2i}[\mathcal{E}^*(z, r)\partial\mathcal{E}/\partial r - \mathcal{E}(z, r)\partial\mathcal{E}^*/\partial r] = |\mathcal{E}(z, r)|^2\partial\Phi/\partial r$  for  $\mathcal{E}(z, r) = |\mathcal{E}(z, r)|\exp[i\Phi(z, r)]$ ; negative (red) and positive (blue) values represent inward and outward flux, respectively [44].

parameters was thus governed by the constraints of avoiding these situations; that is, we selected the geometric beam parameters  $w_0$  and  $r_0$  to fix the focal distance at 1 km while keeping a relatively large ring width, allowing for the peak intensity to remain below ionization threshold until the final convergence stage. The collapse distance indeed scales as  $w_0^2$  and could therefore be postponed beyond the position of the autofocus. Then we selected a truncation factor  $\alpha = 0.05$ , for which the power content of the primary ring  $P_1$  is equal to  $0.4P_{in}$ , allowing us to perform simulations for beam powers such that the power content of the primary ring reaches up to 10 critical powers for self-focusing  $P_{cr}$ . This is a large value that usually leads to the self-focusing and collapse of bell-shaped beams. However, due to the distribution of power over a ring, an almost linear propagation is preserved until the focal region is approached and the abrupt stage of autofocusing begins. At this point, the ring collapse into a bell-shaped beam, and the process is further accelerated by Kerr self-focusing. Figure 2 shows the general features of ring-Airy beam propagation up to the focal region for a beam with moderate input power  $P_{in} < P_{cr}$ . As shown in Fig. 2(a), the boundary  $r_1(z)$  of the primary ring is determined by calculating the first local minimum beyond the first local maximum of the intensity profile along the radius and varies with the propagation distance. The power content  $P_1(z)$  in the primary ring is thus evaluated by

$$P_1(z) = \int_0^{r_1(z)} 2\pi r |\mathcal{E}(r, z)|^2 dr. \quad (5)$$

The ring-Airy beam automatically focuses during linear propagation, while  $P_1$  decreases slightly with increasing propagation distance [Fig. 2(b)]. This decrease is a result of the truncation of the Airy beam tail by the exponential function. The nontruncated Airy beam indeed exhibits a balanced power flux with inward and outward components sustaining the power content in every ring. Closer to the focal region, a spiky

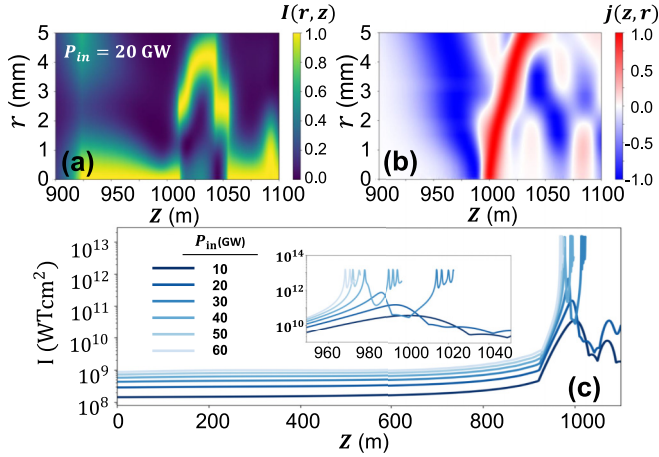


FIG. 3. Ring-Airy beam propagation for input powers up to 70 GW. Evolution of (a) the amplitude, (b) the energy current density (red = inward, blue = outward), and (c) on-axis intensity of the field as a function of propagation distance  $z$ .

feature is observed for  $P_1(z)$ . It corresponds to a reorganization stage of the ring pattern during which the ring converges and starts forming a bell-shaped beam. As the primary ring disappears, the numerical determination of  $r_1(z)$  and of  $P_1$  undergoes a discontinuity. Figure 3 shows how the beam profile evolves around the nonlinear focus for the input power  $P_{in} = 20$  GW. The amplitude distribution [Fig. 3(a)] shows the effect of nonlinear self-focusing at 1 km. Compared with Fig. 2(d), the energy current exhibits an enhanced contrast between the inward and outward power fluxes: near the nonlinear focus, diffraction and defocusing nonlinearity promote a transition from an inward to an outward energy flow over a shorter length scale. Figure 3(c) shows the maximum intensity of the radial beam profile  $\max_r(|\mathcal{E}(z, r)|^2)$  as a function of propagation distance  $z$  for different input powers  $P_{in}$ . Propagation is almost linear, with a maximum intensity below the ionization threshold up to the nonlinear focus. When the beam approaches the focus, the intensity contrast becomes sharper for larger input powers. However, filamentation is obtained only for input powers above 25 GW. For input powers between 25 and 40 GW, the nonlinear focus corresponds to a local intensity maximum, but the clamped intensity characterizing a filament [45] is reached only a few meters beyond the nonlinear focus. In this range of input powers, the inward power flux carried by the primary ring leads to a bell-shaped beam with power in excess of  $P_{cr}$  while remaining too weak to induce a collapse, as a certain collapse distance is required that depends on the power content and convergence of the beam. Hence, filamentation does not start before an additional power flux, for instance, from the second ring, converges to the center. When  $P_{in}$  exceeds 40 GW, a sudden intensity buildup occurs and leads to filamentation starting from the nonlinear focus. We note that the position of the nonlinear focus, whether it coincides with the beginning of filamentation or not, shifts to shorter distances as the input power increases.

By increasing the power of the input beam while keeping its maximum intensity below ionization threshold, we increase the power contained in the primary ring, thus further enhancing the final self-focusing and collapse of the bell-

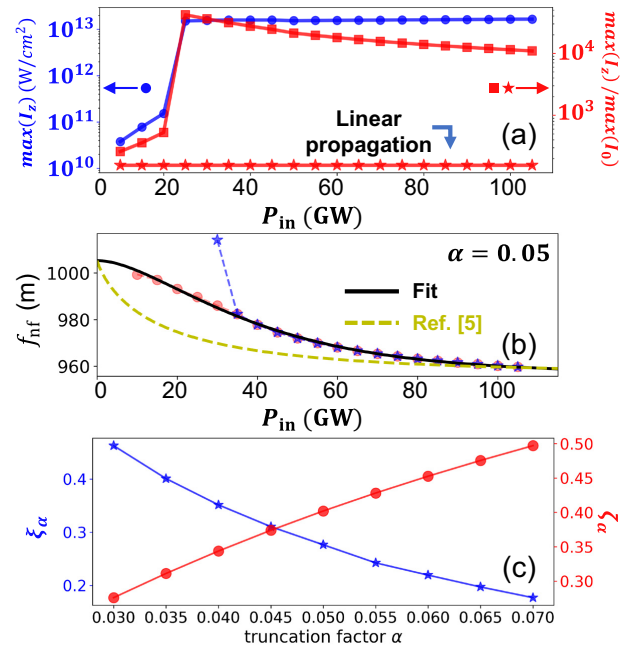


FIG. 4. (a) Maximum intensity (blue curve with circles) reached during forward propagation and peak intensity contrast (red curve with diamonds) as a function of input power  $P_{in}$ . For comparison, the peak intensity contrast for linear propagation is also plotted with red stars. (b) Nonlinear focus shift (red curve and circles) and position of maximum intensity (blue curve and stars) as a function of the input power; the black solid line denotes the fitting by Eq. (6) with  $\alpha = 0.05$ ; the yellow dashed line represents the fitting directly using the expression in Ref. [5]. See the Appendix for fitting with other truncation factors. (c) Fitting parameters  $\xi_\alpha$  (blue curve and stars) and  $\zeta_\alpha$  (red curve and circles) as a function of the truncation factor  $\alpha$ .

shaped beam resulting from the convergence of the primary ring. Higher-order effects then become relevant and prevent collapse. Beyond this point a filament is generated on axis.

As shown in Fig. 4, the maximum intensity contrast is enhanced by two orders of magnitude compared to the case of linear propagation of a ring-Airy beam. In our simulations, the contrast increases from 150 to 80 000 by increasing the input power above the filamentation threshold. For larger input powers, plasma defocusing and MPA efficiently clamp the peak intensity at the same value ( $\sim 20$  TW/cm<sup>2</sup>), and the contrast drops, simply reflecting the increase of the peak intensity of the input beam. Figure 4(b) shows the shift of the nonlinear focus as a function of the input power  $P_{in}$  for the truncation factor  $\alpha = 0.05$ . As mentioned earlier, the filament starts a few tens of meters beyond the nonlinear focus for moderate values of  $P_{in}$  and from the nonlinear focus for higher powers.

Both the position of the nonlinear focus and the filament starting point are decreasing functions of the input power  $P_{in}$ , or the power content of the primary ring  $P_1(\alpha) \equiv \gamma_\alpha P_{in}$ , and decreasing functions of  $\alpha$  as well, in keeping with the fact that lower values of the truncation factor are associated with a higher inward power flux. Note that to facilitate the comparison of results obtained with different values for  $\alpha$ , the input power is adjusted such that the power content of the primary ring  $P_1$  remains the same across all values of  $\alpha$ . In

TABLE II. Truncation factor  $\alpha$ ,  $g(\alpha)$ , and  $\gamma_\alpha \equiv P_1/P_{in}$  when  $r_0/w_0 = 15$ .

Parameter	Value	Value	Value	Value	Value	Value	Value	Value	Value
$\alpha$	0.030	0.035	0.040	0.045	0.050	0.055	0.060	0.065	0.070
$g(\alpha)$	0.987	0.983	0.980	0.974	0.968	0.964	0.957	0.954	0.949
$\gamma_\alpha$	0.276	0.311	0.344	0.374	0.402	0.428	0.453	0.475	0.497

detail, we take  $\alpha = 0.05$  as the reference value; by specifying the range of input power  $P_{in}$  from 10 to 110 GW we then calculate the power content of the primary ring  $P_1(\alpha = 0.05)$ . Then we adjust the input power for other truncation factors  $\alpha$  through  $P_{in}(\alpha = 0.05) \equiv P_1(\alpha = 0.05)/\gamma_\alpha$ , so that  $P_1(\alpha) = \gamma_\alpha P_{in}(\alpha) = P_1(\alpha = 0.05)$ .

Panagiotopoulos *et al.* investigated the nonlinear propagation dynamics of ring-Airy beams in condensed media over short distances (approximately centimeter scales) [5,34,42] and proposed an empirical formula predicting the nonlinear focus shift. In our simulations, we observed a similar dynamics for the propagation of ring-Airy beams over kilometer scales, but the empirical formula for the nonlinear focus shift had to be adapted to these distances.

The following empirical law for the position of the nonlinear focus  $f_{nf}$  matches our simulation results accurately:

$$f_{nf} = f - (f - f_{min}) \left\{ 1 - \exp \left( - \left[ \zeta_\alpha \frac{\gamma_\alpha P_{in}}{P_{cr}} \right]^{\xi_\alpha} \right) \right\}^2, \quad (6)$$

where  $f \equiv 4z_R \sqrt{1 + r_0/w_0}$  is the linear focus;  $f_{min} = f \sqrt{1 - 1.5w_0/R_0}$  is the estimated propagation distance, in which  $R_0 \equiv r_0 - w_0 g(\alpha)$  is the radial location of the first intensity maximum of the ring-Airy beam; and  $\gamma_\alpha \equiv P_1(\alpha)/P_{in}$ . The exact values of  $g(\alpha)$  and  $\gamma_\alpha$  when  $r_0/w_0 = 15$  can be found in Table II. The fit is valid only up to a power limit ( $P_{in} < 100$  GW) as ring-Airy beams with larger power do self-focus and collapse onto a singular ring before reaching a nonlinear focus. Thus, at larger powers, the nonlinear focus shift and the starting point of the filament will deviate from the trend given by Eq. (6). In the fitting function of  $f_{nf}$ , we also introduce an additional parameter  $\zeta_\alpha$  and a coefficient  $\xi_\alpha$  in the exponent for better fitting. Figure 4(c) shows the quantities  $\xi_\alpha$  and  $\zeta_\alpha$ , extracted from numerical simulation results, as a function of the truncation factor  $\alpha$  that controls how much energy from the tail of the beam can be transferred to the center.  $\xi_\alpha$  is a monotonic decreasing function with increasing  $\alpha$ . The inward power flux from the tail of the ring-Airy beam diminishes, and the power of the primary ring undergoes a comparatively stronger diffraction. This results in the decrease of  $\xi_\alpha$  for larger  $\alpha$ , which means that the nonlinear focus will shift as a function of the input power at a slower rate. Correspondingly, when  $\alpha$  increases, the numerator  $\zeta_\alpha \gamma_\alpha P_{in}$  in the exponent must increase in order to observe a nonlinear focus shift of the same scale as that obtained for small  $\alpha$ . Although  $\gamma_\alpha$  increases with  $\alpha$ , it is not enough to counter balance the decrease in  $\xi_\alpha$ . So in the fitted equation, our coefficient  $\zeta_\alpha$  also increases as  $\alpha$  increases, as shown in Fig. 4(c). From the transverse beam profile shown in Fig. 5(a), we characterized the diameter of  $\approx 100 \mu\text{m}$  for the filament after it is formed ( $z > 973$  m). As can be seen from Fig. 5, regardless of the input power, the maximum power contained in a cylinder with

a radius of  $100 \mu\text{m}$  is  $\sim 3$  GW, i.e., about  $P_{cr}$ , and the same order of magnitude is obtained for the power contained in cylinders with larger radii of 0.5 or 1 mm, even if the power in the primary ring of the input beam is 10 times larger. This result is in keeping with early observations of filaments in air [46] and is mainly due to intensity clamping within the filament [45], a phenomenon that depends on neither the input beam shape nor the propagation history.

#### IV. CONCLUSION

In conclusion, we have studied the nonlinear propagation dynamics of finite-energy ring-Airy beams at kilometer scales

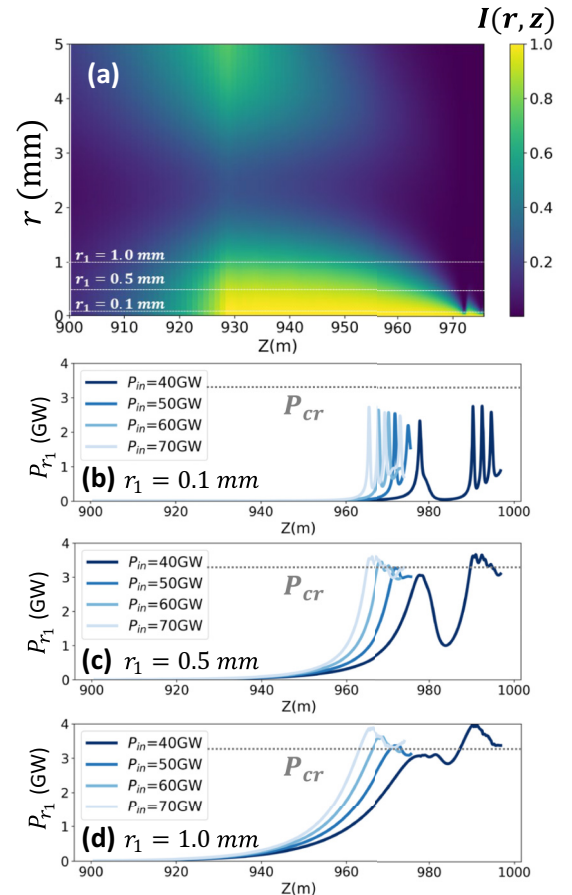


FIG. 5. (a) Detailed view of the intensity profile  $I(r, z)$  near the nonlinear focus ( $z \sim 973$  m) when  $P_{in} = 50$  GW. Power contained in a beam section with a radius of (b)  $100 \mu\text{m}$ , corresponding to the filament, (c)  $0.5$  mm, and (d)  $1$  mm as a function of propagation distance for different input powers. The value of the critical power  $P_{cr} \sim 3.2$  GW is also plotted as a gray dashed line in (b)–(d). The power  $P_{r1}$  is calculated using Eq. (5) by replacing the upper limit of the integral with  $r_1 = 0.1, 0.5, 1.0$  mm.

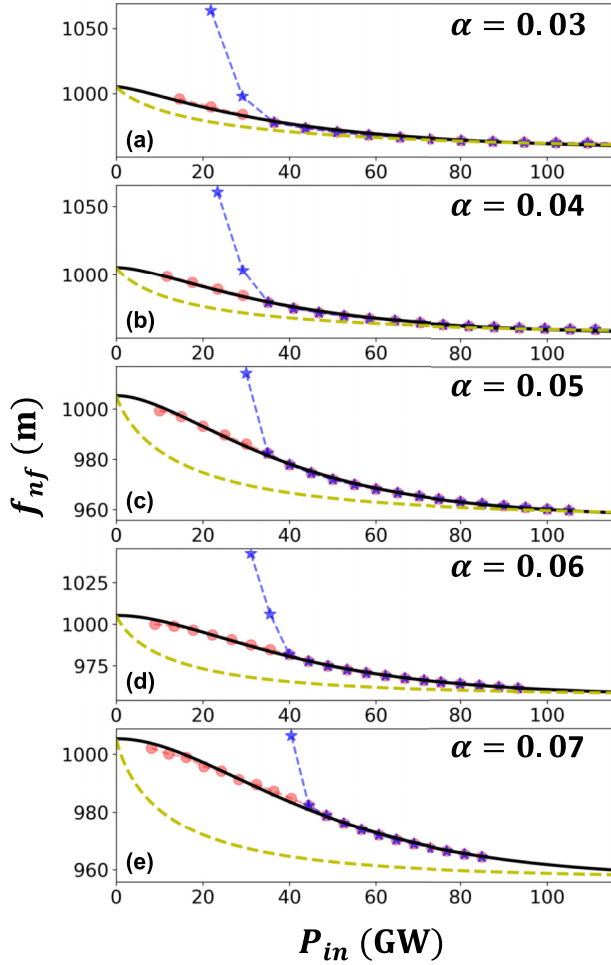


FIG. 6. (a)–(e) Simulation results for different truncation factors  $\alpha = 0.03$ – $0.07$ . The notation for each line is the same as in Fig. 4(b).

in air. By numerically solving the NLSE, we found that for a range of input powers up to  $\sim 30 P_{\text{cr}}$ , a ring-Airy beam propagates quasilinearly until the primary ring forms a bell-shaped beam whose convergence is accelerated as it experiences a short self-focusing stage up to a nonlinear focus. The position of the nonlinear focus is shifted to shorter distances as the input power increases. The nonlinear focus shift is also influenced by the apodization of the ring-Airy beam as its larger shifts are obtained for small truncation factors, corresponding to weakly apodized beams with a stronger inward power flux. We have proposed an empirical formula that reproduces the nonlinear focus shift obtained in numerical simulations over a range of powers above  $P_{\text{cr}}$ , thus predicting the position of the starting point of filamentation and the highest intensity. Beyond this point, a plasma string is generated by the pulse, whose highly nonlinear dynamics cannot be described by our model. Nevertheless, our results show that the power localized in the filament and in a cylindrical region 10 times wider than the filament diameter is roughly  $P_{\text{cr}}$ , and therefore, the plasma string formed at the nonlinear focus cannot be extended farther than a few tens of centimeters. In contrast to the projection scheme based on Bessel beams, the length and uniformity of the plasma string are here limited by the power threshold above which the primary ring undergoes a

singular ring collapse before the nonlinear focus is reached. Hence, the interest of the present projection scheme based on ring-Airy beams lies in its ability to deliver a power density of  $20 \text{ TW/cm}^2$  on a target located at kilometeric distances. Several effects that we did not consider in this paper could limit the capacity of this projection scheme: (i) Dispersion in air stretches the pulse duration during its propagation. However, this effect can be precompensated by using negatively chirped pulses. (ii) The ring-Airy beam could break up into multiple beamlets before reaching the focus by Kerr-induced modulational instability. However, compared to bell-shaped beams with similar powers, ring beams are less prone to this instability because the power of the main lobe is distributed over a much larger surface, leading to smaller instability growth rates. (iii) Turbulence in air could affect the accuracy of this projection scheme. While this point deserves further study, the linear propagation of circular-Airy beams over 1000 m in atmospheric turbulence was investigated by Wang Xiaozhang *et al.* [47]. The results show that the drift of the autofocus in the transverse plane is about  $8 \mu\text{m}$ , with  $C_n^2$  ranging from  $1 \times 10^{-15}$  to  $30 \times 10^{-15} \text{ m}^{-2/3}$ , while the position of the autofocus length is almost the same. Since the position of the autofocus in our simulations is mainly governed by linear effects, while nonlinear effects play a more important role close to the focus, we expect that atmospheric turbulence will lead to a relatively small beam wandering of the focal spot in the transverse plane.

It is worth noting that the input powers required to initiate filamentation in air at a distance of 1 km using a ring-Airy beam require only tens of gigawatts, which is at least one order of magnitude lower than the terawatt laser pulses used in previous works [48–52]. We hope our findings will contribute to the development of laser beam and pulse shaping for the transmission of high laser energy densities to remote targets in the atmosphere and related atmospheric applications.

## ACKNOWLEDGMENTS

L.Z. has been supported by the Zhiyuan Honors Doctoral Program of Shanghai Jiao Tong University.

## APPENDIX

In this Appendix, we show in detail how we fit the simulation result of the nonlinear focus shift. By fixing the truncation factor  $\alpha$ , we ran several simulations with varying input powers  $P_{\text{in}}(\alpha)$ . We have different sets of  $P_{\text{in}}$  across each  $\alpha$ . This ensures that the power content in the primary ring remains the same,  $P_1(\alpha) = \gamma_\alpha P_{\text{in}}(\alpha) = P_1(\alpha = 0.05)$ , where we have taken  $\alpha = 0.05$  as the reference case. In the simulation, we would like to study the propagation dynamics with different truncation factors  $\alpha$  while keeping the set of the power content  $P_{\text{in}}$  in the primary ring the same. In detail, we first select the truncation factor  $\alpha$  to be 0.05 and a set of input power  $P_{\text{in}}$  from 10 to 110 GW. Then, we calculate the power content contained in the primary ring  $P_1(\alpha = 0.05) = \gamma_\alpha P_{\text{in}}(\alpha = 0.05) = \gamma_\alpha P_{\text{in}}(\alpha = 0.05)$ . Therefore, this variable  $P_1(\alpha = 0.05)$  is also a finite set. When we change  $\alpha$  to another value, we calculate the corresponding set of input power  $P_{\text{in}}$  based on

the set of  $P_1$  ( $\alpha = 0.05$ ) and run the simulation. So the set of input power  $P_{in}$  is different for different  $\alpha$ , while the set of  $P_1$  is the same. In Fig. 6, we show the simulation results for  $\alpha = 0.03, 0.04, 0.05, 0.06, 0.07$ . The nonlinear focus shift (red curve with circles) and the position of the maximum intensity

(blue curve with stars) are plotted as a function of the input power; the black solid line denotes the fitting by Eq. (6) in the main text. The coefficients  $\zeta_\alpha$  and  $\xi_\alpha$  are extracted through the fitting process. The yellow dashed lines represent the fitting directly using Eq. (2) in Ref. [5].

- [1] N. K. Efremidis and D. N. Christodoulides, Abruptly autofocusing waves, *Opt. Lett.* **35**, 4045 (2010).
- [2] D. G. Papazoglou, N. K. Efremidis, D. N. Christodoulides, and S. Tzortzakis, Observation of abruptly autofocusing waves, *Opt. Lett.* **36**, 1842 (2011).
- [3] P. Polynkin, M. Kolesik, J. V. Moloney, G. A. Siviloglou, and D. N. Christodoulides, Curved plasma channel generation using ultraintense airy beams, *Science* **324**, 229 (2009).
- [4] P. Polynkin, M. Kolesik, and J. Moloney, Filamentation of Femtosecond Laser Airy Beams in Water, *Phys. Rev. Lett.* **103**, 123902 (2009).
- [5] P. Panagiotopoulos, D. G. Papazoglou, A. Couairon, and S. Tzortzakis, Sharply autofocused ring-airy beams transforming into non-linear intense light bullets, *Nat. Commun.* **4**, 2622 (2013).
- [6] A. D. Koulouklidis, D. G. Papazoglou, V. Y. Fedorov, and S. Tzortzakis, Phase Memory Preserving Harmonics from Abruptly Autofocusing Beams, *Phys. Rev. Lett.* **119**, 223901 (2017).
- [7] K. Liu, A. D. Koulouklidis, D. G. Papazoglou, S. Tzortzakis, and X.-C. Zhang, Enhanced terahertz wave emission from air-plasma tailored by abruptly autofocusing laser beams, *Optica* **3**, 605 (2016).
- [8] P. Zhang, J. Prakash, Z. Zhang, M. S. Mills, N. K. Efremidis, D. N. Christodoulides, and Z. Chen, Trapping and guiding microparticles with morphing autofocusing airy beams, *Opt. Lett.* **36**, 2883 (2011).
- [9] W. Lu, X. Sun, H. Chen, S. Liu, and Z. Lin, Abruptly autofocusing property and optical manipulation of circular airy beams, *Phys. Rev. A* **99**, 013817 (2019).
- [10] Y. Liang, G. Liang, Y. Xiang, J. Lamstein, R. Gautam, A. Bezryadina, and Z. Chen, Manipulation and Assessment of Human Red Blood Cells with Tunable “Tug-of-War” Optical Tweezers, *Phys. Rev. Appl.* **12**, 064060 (2019).
- [11] F. Lu, H. Wu, Y. Liang, L. Tan, Z. Tan, X. Feng, Y. Hu, Y. Xiang, X. Hu, Z. Chen, and J. Xu, Bessel-modulated autofocusing beams for optimal trapping implementation, *Phys. Rev. A* **104**, 043524 (2021).
- [12] M. Manousidaki, D. G. Papazoglou, M. Farsari, and S. Tzortzakis, Abruptly autofocusing beams enable advanced multiscale photo-polymerization, *Optica* **3**, 525 (2016).
- [13] Y. Hu, P. Zhang, C. Lou, S. Huang, J. Xu, and Z. Chen, Optimal control of the ballistic motion of airy beams, *Opt. Lett.* **35**, 2260 (2010).
- [14] J. A. Davis, D. M. Cottrell, and D. Sand, Abruptly autofocusing vortex beams, *Opt. Express* **20**, 13302 (2012).
- [15] Y. Jiang, K. Huang, and X. Lu, Propagation dynamics of abruptly autofocusing airy beams with optical vortices, *Opt. Express* **20**, 18579 (2012).
- [16] P. Li, S. Liu, T. Peng, G. Xie, X. Gan, and J. Zhao, Spiral autofocusing airy beams carrying power-exponent-phase vortices, *Opt. Express* **22**, 7598 (2014).
- [17] X. Zhang, P. Li, S. Liu, B. Wei, S. Qi, X. Fan, S. Wang, Y. Zhang, and J. Zhao, Autofocusing of ring airy beams embedded with off-axial vortex singularities, *Opt. Express* **28**, 7953 (2020).
- [18] Y. Jiang, W. Yu, X. Zhu, and P. Jiang, Propagation characteristics of partially coherent circular airy beams, *Opt. Express* **26**, 23084 (2018).
- [19] T. Li, D. Li, X. Zhang, K. Huang, and X. Lu, Partially coherent radially polarized circular airy beam, *Opt. Lett.* **45**, 4547 (2020).
- [20] T. Li, X. Zhang, K. Huang, and X. Lu, Experimental generation of partially coherent circular airy beams, *Opt. & Laser Technol.* **137**, 106814 (2021).
- [21] W. Lu, H. Chen, S. Liu, and Z. Lin, Rigorous full-wave calculation of optical forces on dielectric and metallic microparticles immersed in a vector airy beam, *Opt. Express* **25**, 23238 (2017).
- [22] W. Lu, X. Sun, H. Chen, S. Liu, and Z. Lin, Optical manipulation of chiral nanoparticles in vector airy beam, *J. Opt.* **20**, 125402 (2018).
- [23] W. Lu, H. Chen, S. Guo, S. Liu, and Z. Lin, Selectively transporting small chiral particles with circularly polarized airy beams, *Opt. Lett.* **43**, 2086 (2018).
- [24] S. Liu, M. Wang, P. Li, P. Zhang, and J. Zhao, Abrupt polarization transition of vector autofocusing airy beams, *Opt. Lett.* **38**, 2416 (2013).
- [25] D. Ye, X. Peng, M. Zhou, Y. Xin, and M. Song, Simulation of generation and dynamics of polarization singularities with circular airy beams, *J. Opt. Soc. Am. A* **34**, 1957 (2017).
- [26] M. Chen, S. Huang, and W. Shao, Tight focusing of radially polarized circular airy vortex beams, *Opt. Commun.* **402**, 672 (2017).
- [27] M. Goutsoulas and N. K. Efremidis, Precise amplitude, trajectory, and beam-width control of accelerating and abruptly autofocusing beams, *Phys. Rev. A* **97**, 063831 (2018).
- [28] T. Geng and X. Zhang, Propagation properties of the circular airy beam with a gaussian envelope in fourier space, *Opt. Express* **28**, 2447 (2020).
- [29] J. Zhang, Y. Li, Z. Tian, and D. Lei, Controllable autofocusing properties of conical circular airy beams, *Opt. Commun.* **391**, 116 (2017).
- [30] D. Mansour and D. G. Papazoglou, Tailoring the focal region of abruptly autofocusing and autodefocusing ring-airy beams, *OSA Continuum* **1**, 104 (2018).
- [31] W. Lu, H. Chen, S. Liu, and Z. Lin, Circular airy beam with an arbitrary conical angle beyond the paraxial approximation, *Phys. Rev. A* **105**, 043516 (2022).
- [32] M. Manousidaki, V. Y. Fedorov, D. G. Papazoglou, M. Farsari, and S. Tzortzakis, Ring-airy beams at the wavelength limit, *Opt. Lett.* **43**, 1063 (2018).
- [33] Y. Wang and Y. Jiang, Dual autofocusing circular airy beams with different initial launch angles, *J. Quant. Spectrosc. Radiat. Transfer* **278**, 108010 (2022).



- [34] P. Panagiotopoulos, A. Couairon, M. Kolesik, D. G. Papazoglou, J. V. Moloney, and S. Tzortzakis, Nonlinear plasma-assisted collapse of ring-airy wave packets, *Phys. Rev. A* **93**, 033808 (2016).
- [35] Q. Jiang, Y. Su, Z. Ma, Y. Li, and W. Zheng, Nonlinear manipulation of circular airy beams, *Appl. Phys. B* **125**, 105 (2019).
- [36] M. V. Berry and N. L. Balazs, Nonspreading wave packets, *Am. J. Phys.* **47**, 264 (1979).
- [37] M. Abramowitz, *Handbook of Mathematical Functions, with Formulas, Graphs, and Mathematical Tables* (Dover, New York, 1974).
- [38] M. D. Feit and J. A. Fleck, Effect of refraction on spot-size dependence of laser-induced breakdown, *Appl. Phys. Lett.* **24**, 169 (1974).
- [39] L. Zou, C. Sun, Y. Rao, T. Sun, J. Yu, and A. Couairon, Reverse wavefront engineering for remote generation of a near-infrared femtosecond bessel beam filament in air, *Phys. Rev. Res.* **4**, 043025 (2022).
- [40] A. Couairon, E. Brambilla, T. Corti, D. Majus, O. de J. Ramírez-Góngora, and M. Kolesik, Practitioner's guide to laser pulse propagation models and simulation, *Eur. Phys. J.: Spec. Top.* **199**, 5 (2011).
- [41] J. Marburger, Self-focusing: Theory, *Prog. Quantum Electron.* **4**, 35 (1975).
- [42] P. Panagiotopoulos, D. Abdollahpour, A. Lotti, A. Couairon, D. Faccio, D. G. Papazoglou, and S. Tzortzakis, Nonlinear propagation dynamics of finite-energy airy beams, *Phys. Rev. A* **86**, 013842 (2012).
- [43] G. Fibich, N. Gavish, and X.-P. Wang, Singular ring solutions of critical and supercritical nonlinear Schrödinger equations, *Phys. D (Amsterdam, Neth.)* **231**, 55 (2007).
- [44] P. Polesana, M. Franco, A. Couairon, D. Faccio, and P. Di Trapani, Filamentation in Kerr media from pulsed Bessel beams, *Phys. Rev. A* **77**, 043814 (2008).
- [45] J. Kasparian, R. Sauerbrey, and S. Chin, The critical laser intensity of self-guided light filaments in air, *Appl. Phys. B* **71**, 877 (2000).
- [46] A. Braun, G. Korn, X. Liu, D. Du, J. Squier, and G. Mourou, Self-channeling of high-peak-power femtosecond laser pulses in air, *Opt. Lett.* **20**, 73 (1995).
- [47] Wang Xiaozhang, T. Feng, Y. Mengjie, L. Rui, D. Dejun, Z. Hui, and C. Ruining, Experimental simulation of circular-airy beam drift in atmospheric turbulence, *Chin. J. Lasers* **42**, 0813001 (2015).
- [48] A. Houard *et al.*, Laser-guided lightning, *Nat. Photonics* **17**, 231 (2023).
- [49] G. Méchain, C. D'Amico, Y.-B. André, S. Tzortzakis, M. Franco, B. Prade, A. Mysyrowicz, A. Couairon, E. Salmon, and R. Sauerbrey, Range of plasma filaments created in air by a multi-terawatt femtosecond laser, *Opt. Commun.* **247**, 171 (2005).
- [50] M. Durand, A. Houard, B. Prade, A. Mysyrowicz, A. Durécu, B. Moreau, D. Fleury, O. Vasseur, H. Borchert, K. Diener, R. Schmitt, F. Théberge, M. Chateaufneuf, J.-F. Daigle, and J. Dubois, Kilometer range filamentation, *Opt. Express* **21**, 26836 (2013).
- [51] J. Kasparian, R. Ackermann, Y.-B. André, G. Méchain, G. Méjean, B. Prade, P. Rohwetter, E. Salmon, K. Stelmazczyk, J. Yu, A. Mysyrowicz, R. Sauerbrey, L. Wöste, and J.-P. Wolf, Electric events synchronized with laser filaments in thunderclouds, *Opt. Express* **16**, 5757 (2008).
- [52] A. Goffin, I. Larkin, A. Tartaro, A. Schweinsberg, A. Valenzuela, E. W. Rosenthal, and H. M. Milchberg, Optical Guiding in 50-Meter-Scale Air Waveguides, *Phys. Rev. X* **13**, 011006 (2023).